



Article

Silicon–Nanodiamond-Based Anode for a Lithium-Ion Battery

Cheng-Ying Jhan, Shi-Hong Sung and Yonhua Tzeng *

Institute of Microelectronics, Department of Electrical Engineering, National Cheng Kung University, One University Road, Tainan 70101, Taiwan; m10506126@gmail.com (C.-Y.J.); william8945@gmail.com (S.-H.S.)

* Correspondence: tzengyo@mail.ncku.edu.tw

Abstract: Maintaining the physical integrity of a silicon-based anode, which suffers from damage caused by severe volume changes during cycling, is a top priority in its practical applications. The performance of silicon-flake-based anodes has been significantly improved by mixing nanodiamond powders with silicon flakes for the fabrication of anodes for lithium-ion batteries (LIBs). Nanodiamonds adhere to the surfaces of silicon flakes and are distributed in the binder between flakes. A consistent and robust solid electrolyte interphase (SEI) is promoted by the aid of abundant reactive surface-linked functional groups and exposed dangling bonds of nanodiamonds, leading to enhanced physical integrity of the silicon flakes and the anode. The battery's high-rate discharge capabilities and cycle life are thus improved. SEM, Raman spectroscopy, and XRD were applied to examine the structure and morphology of the anode. Electrochemical performance was evaluated to demonstrate a capacity retention of nearly 75% after 200 cycles, with the final specific capacity exceeding 1000 mAh/g at a test current of 4 mA/cm². This is attributed to the improved stability of the solid electrolyte interphase (SEI) structure that was achieved by integrating nanodiamonds with silicon flakes in the anode, leading to enhanced cycling stability and rapid charge-discharge performance. The results from this study present an effective strategy of achieving high-cycling-performance by adding nanodiamonds to silicon-flake-based anodes.

Keywords: silicon; anode; nanodiamond; battery; SEI



Citation: Jhan, C.-Y.; Sung, S.-H.; Tzeng, Y. Silicon–Nanodiamond-Based Anode for a Lithium-Ion Battery. *Nanomaterials* **2024**, *14*, 43. <https://doi.org/10.3390/nano14010043>

Academic Editor: Carlos Miguel Costa

Received: 4 December 2023

Revised: 15 December 2023

Accepted: 20 December 2023

Published: 22 December 2023



Copyright: © 2023 by the authors. Licensee MDPI, Basel, Switzerland. This article is an open access article distributed under the terms and conditions of the Creative Commons Attribution (CC BY) license (<https://creativecommons.org/licenses/by/4.0/>).

1. Introduction

Lithium-ion batteries (LIBs) are one of the most important energy storage devices in modern history. They exhibit high energy efficiency and lightweight properties [1–3]. However, the rapid evolution of mobile electronics, electric vehicles, and high-power renewable energy technologies has caused the demand for enhanced capacity retention, energy density, lifespan, safety, and cost reduction to rise beyond the limits of state-of-the-art LIB technology [4–7].

Technological advancement in LIB anode (negative electrode) materials has focused primarily on augmenting the electrode's capacity. Artificial graphite (AG) remains the dominant negative electrode material used in lithium-ion batteries [8]. However, current AG technology has approached a theoretical capacity limit of 372 mAh/g [9], which is insufficient for the high demands of current power cells. Hence, the development of high-capacity materials such as silicon-based negative electrodes has garnered attention.

Silicon exhibits a theoretical capacity as high as 3579 milliampere-hours per gram (mAh/g) and demonstrates an ideal lithium insertion potential (<0.5 V) [10]. Utilizing silicon as a negative electrode material shows promise for achieving energy densities surpassing 500 watt-hours per kilogram (Wh/kg) [11]. Nevertheless, practical applications of silicon electrodes face several challenges, including significant volume expansion (300–400%) and an unstable solid electrolyte interphase (SEI) [12]. The volume expansion and interphase instability of silicon–carbon anode materials have been extensively studied [13,14]. Nanoscale silicon powder reduces the effects of volume expansion. However, the high cost of nanoscale silicon particles restricts their widespread usage. High-quality

silicon flake waste, a byproduct of the semiconductor industry, offers a suitable raw material for silicon anode manufacturing owing to its abundance, low cost, and recyclable nature [15]. However, the utilization of inexpensive and abundant micrometer-sized silicon flakes faces significant challenges during charge–discharge cycles owing to slow ion diffusion kinetics and notable volume expansion effects [12,16].

Several efforts have been made to suppress irreversible chemical reactions between the electrolyte and the anode, including the application of protective surface coatings such as carbon [17–19], lithium benzoate [20], polymers [21], and Al_2O_3 [22]. However, the performance of anode electrodes employing these coating materials fails to meet all of the optimal aspects of structural stability, powder filling, and conductivity required for commercial demands. Notably, in lithium-ion batteries, developing a new coating material is crucial to suppress solid electrolyte interphase (SEI) formation, maintain mechanical integrity during charge–discharge processes, and facilitate rapid electron and lithium-ion conduction. Therefore, we propose a novel strategy of incorporating nanocrystalline diamond (ND) [15] as an additive into the anode. ND exhibits excellent electrochemical and chemical inertness, along with high mechanical strength. On the other hand, the abundant dangling bonds on the surfaces of nanodiamonds allow various functional groups to attach and desirable chemical compounds to form. Other than the surfaces, most nanodiamonds possess relative chemical stability, thereby resisting erosion from various chemical processes, making it a material capable of maintaining stability in various environments [23–26].

In this study, we selected micrometer-sized silicon flakes (about $800\text{ nm} \times 800\text{ nm} \times 100\text{ nm}$ in size) as the anode material, and these flakes boast high theoretical capacity (3579 mAh/g based on $\text{Li}_{3.75}\text{Si}$) and a flat and low charging potential (0–0.5 V vs. Li/Li^+), rendering them promising anode candidates [27,28]. However, micrometer-sized silicon flakes have several common issues, including severe volume changes and low charging potential, leading to the decomposition of organic electrolytes and the formation of a thick solid electrolyte interphase (SEI) layer [29,30]. To demonstrate the effectiveness of ND doping, we conducted an in-depth investigation into the degradation and deterioration of original silicon anodes during cycling. The studied ND-mixed silicon anodes demonstrated their potential to exhibit highly stable long-term cycling performance and reproducibility. Therefore, we employed scanning electron microscopy (SEM), X-ray diffraction (XRD), and electrochemical measurements to study variations in electrode charge–discharge behaviors and phase transitions in the microstructure during lithiation/delithiation processes. Through these observations, we demonstrate the benefits of nanodiamonds in facilitating the formation of a uniform solid electrolyte interphase (SEI). The stable diamond-mixed uniform SEI improved high-rate performance and long-term cycling.

2. Materials and Methods

2.1. Materials

In this research, the silicon material employed was acquired from AUO Crystal Corporation, and measures approximately 800 nm in length and width, with a thickness of around 100 nm. The binder utilized was Poly (acrylic acid; PAA) provided by Eternal Materials Co. (Kaohsiung City, Taiwan), and Super P from Ubiq Technology Co. (San Diego, CA, USA) served as the conductivity enhancement additive. A copper foil with a thickness of 10 μm was selected as the current collector in the electrode fabrication process.

The nanodiamond powder was procured from Taiwan Union Abrasives Corp. (Tainan City, Taiwan). Meanwhile, the battery-grade electrolyte utilized in this investigation was obtained from Hopax Chems., MFG., Co. in Taipei, Taiwan. The electrolyte comprised a 1 M LiPF_6 solution dissolved in equal volumes of ethylene carbonate (EC), diethyl carbonate (DEC), and dimethyl carbonate (DMC). In addition, the electrolyte contained 10 wt.% fluoroethylene carbonate (FEC).

2.2. Preparation of Anode

We uniformly mixed silicon flakes, binders, and conductive agent (Super P) using a weight ratio of 7:2:1. In addition, we incorporated 3 wt.% of solid 10 or 30 nm polycrystalline

nanodiamond powder into the mixture. Once thoroughly mixed, the substance formed the anode slurry. Subsequently, the slurry was coated onto a copper foil with a Dr. blade and dried in a vacuum oven at 80 °C for 8 h. Finally, the samples were cut into electrodes with an area of 1.13 cm².

2.3. Material Characterization

This investigation delved into the physical attributes and arrangement of materials through cutting-edge imaging and spectroscopic methodologies. Scanning electron microscopy (SEM) analysis was conducted utilizing a Hitachi-SU8000 instrument located in Taipei, Taiwan. Operating at an acceleration voltage of 5 kV, SEM provided comprehensive insights into the surface morphology and internal configurations of the materials.

To investigate molecular composition and vibrational characteristics, Raman spectroscopy was employed. The Raman system from Horiba Scientific (Taipei, Taiwan) utilized a green laser emitting light at 532 nm wavelength with a laser power of 450 mW, focused precisely on an area of approximately 10 μm on the sample's surface. Through detailed analysis of Raman spectra, intricate nanostructural information on the sample was unveiled.

XRD (X-ray Diffraction) analysis, facilitated by the D8 DISCOVER with GADDS (Bruker AXS GmbH, Karlsruhe, Germany) at a scanning rate of 4°/min, was instrumental in determining the crystallographic orientation of both the silicon powder and diamond. XRD spectra were collected on a Cu Kα beam line with a wavelength of 1.54184 Å.

In summary, these techniques were instrumental in examining and characterizing the morphology, structure, and properties of the materials under investigation.

2.4. Fabrication of Coin Cells

In an argon-filled glove-box environment that was meticulously controlled to maintain oxygen and moisture levels below 0.5 ppm, the assembly of electrodes into CR2032 coin cells was conducted. Lithium metal was employed as the anode material in this setup. The selected electrolyte consisted of a 1 M LiPF₆ solution dissolved in a blend of ethylene carbonate (EC), diethyl carbonate (DEC), and dimethyl carbonate (DMC), each in equal proportions, resulting in a 1:1:1 volume ratio. Additionally, the electrolyte composition included the incorporation of 10 wt.% fluoroethylene carbonate (FEC).

2.5. Electrode Characterization

STEM and SEM were employed for the characterization of the anodes' morphology and structures. Cycled electrodes were prepared and processed within a glove box following the procedures outlined in the references.

2.6. Test Cells

Galvanostatic discharge/charge experiments were conducted using a BAT battery testing system. The voltage range for the half cell spanned from 0.01 V to 1.5 V. The testing commenced after a resting period of one day. Initially, three cycles were performed at a current density of 0.2 mA/cm² for the half cell, followed by subsequent cycles at 1.0 mA/cm². Cyclic voltammetry (CV) and electrochemical impedance spectroscopy (EIS) measurements were conducted following the methodologies detailed in reference [31]. The CV measurements employed a scanning rate of 0.05 mV/s within a range of 0–1.5 V at room temperature. EIS measurements were recorded over a frequency range of 0.1–100 kHz.

3. Results and Discussion

Figure 1 shows Raman spectra for Si-flake-based and Si-flake–nanodiamond-based Raman spectra. Nanodiamonds of 10 nm and 30 nm in sizes were used. The spectra of reference materials are primarily influenced by the first-order Raman-allowed graphite and diamond Raman scattering modes; i.e., the doubly degenerated E_{2g} at around 1586 cm⁻¹ and the triply degenerated T_{2g} at approximately 1332 cm⁻¹. In the case of the microcrystalline graphite sample, an additional weak feature is observed near 1430 cm⁻¹, corre-

sponding to the disorder-induced “D” line. This particular feature tends to be observed at lower frequencies and exhibits a significantly stronger intensity under conventional visible excitations [32,33]. The characteristic peaks of silicon crystals are clearly shown at wavenumbers of 510 and 960 cm^{-1} [34].

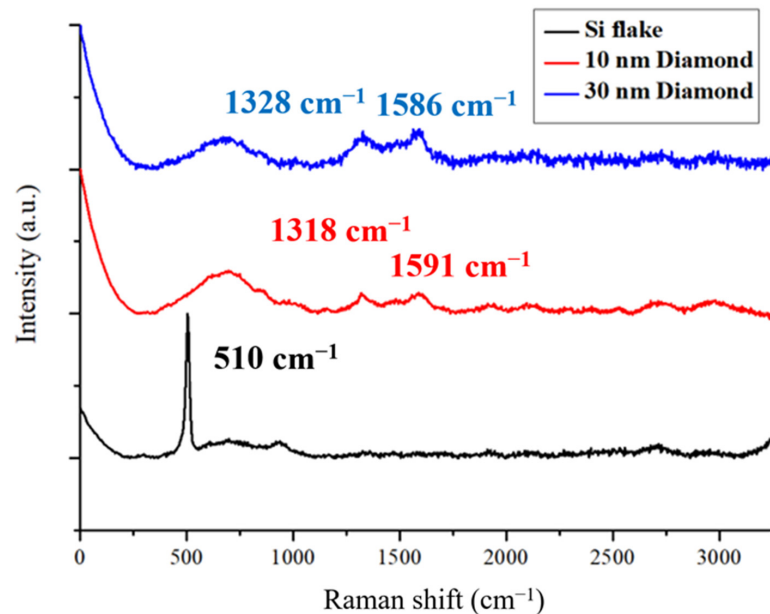


Figure 1. Raman spectra of Si flakes and nanocrystalline diamonds.

Figure 2 illustrates the XRD spectra of silicon powder and nanodiamond powders. A relatively intense diffraction peak at approximately $2\theta \approx 44$ degrees corresponding to the (111) lattice plane signifies that the primary crystalline phase of the diamond powder is (111), although there are orderly arrangements of other planes such as (220), (311), (400), and (331) present as well. Additionally, the diffraction characteristic peaks of nanoscale silicon powder, as analyzed previously, exhibit organized arrangements including (111), (220), (311), (400), and (331) [35,36].

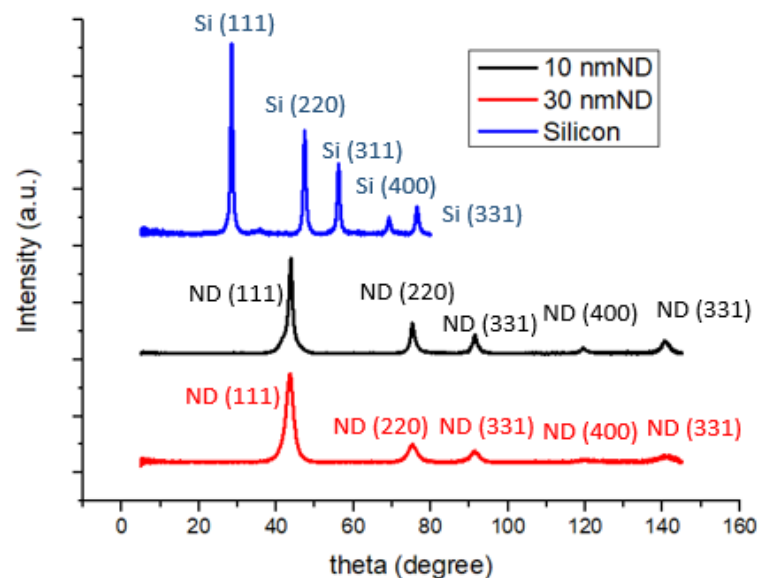


Figure 2. XRD patterns of anodes made of silicon and silicon–nanodiamond mixtures (10 and 30 nm).

Figure 3a,b portray the surface microstructure of a typical silicon anode, revealing irregular silicon flakes of around 800 nm (indicated by the green arrow in Figure 3b)

enveloped by approximately 50 nm spherical conductive agent (Super P, indicated by the red arrow in Figure 3b). The uniform blending of silicon powder and the conductive agent form an effective conductive network. In contrast, Figure 3c,d depicts the surface microstructure of a silicon–nanodiamond anode. Unlike the conventional silicon anode, the surface of nanoscale silicon flake is coated by irregularly shaped polycrystalline diamond particles of approximately 10 nm (small dots indicated by the white arrows in Figure 3d).

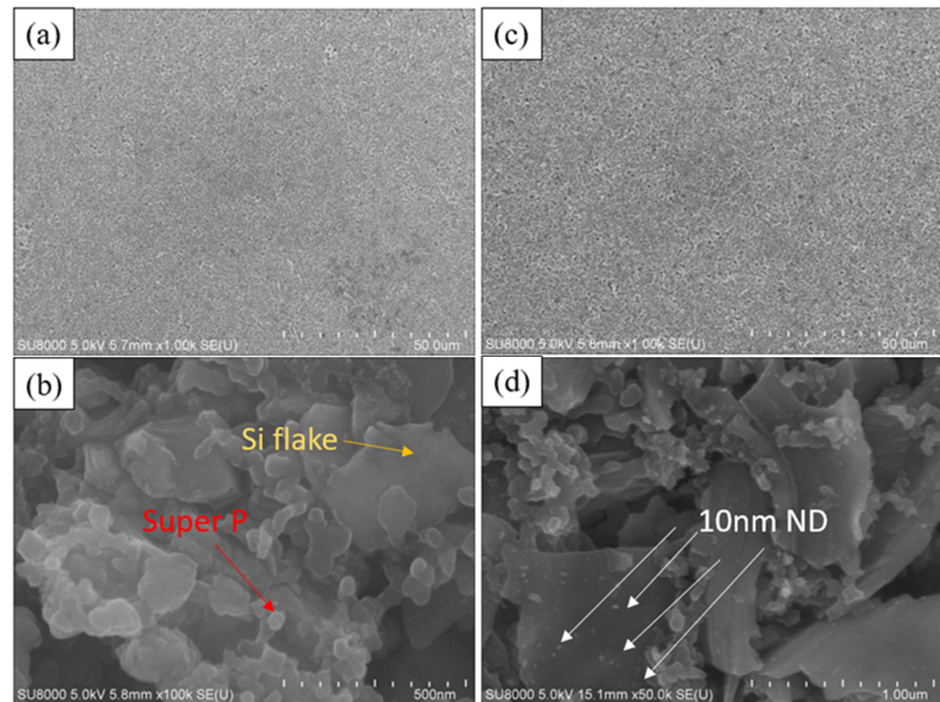


Figure 3. SEM image of the surface of (a,b) Si-based anode and (c,d) Si–nanodiamond-based anode.

We conducted SEM mapping for C, O, and Si, as shown in Figure 4 below. Apart from diamonds, the binder also adheres to the silicon wafer surface. The PAA binder consists primarily of carbon atoms, which makes the identification of diamond by elemental analysis impractical. Directly assessing the distribution based on the size of each material in the images allows for quicker and more accurate analysis (Si flake 800 nm, Super P 50 nm, diamond 10 nm).

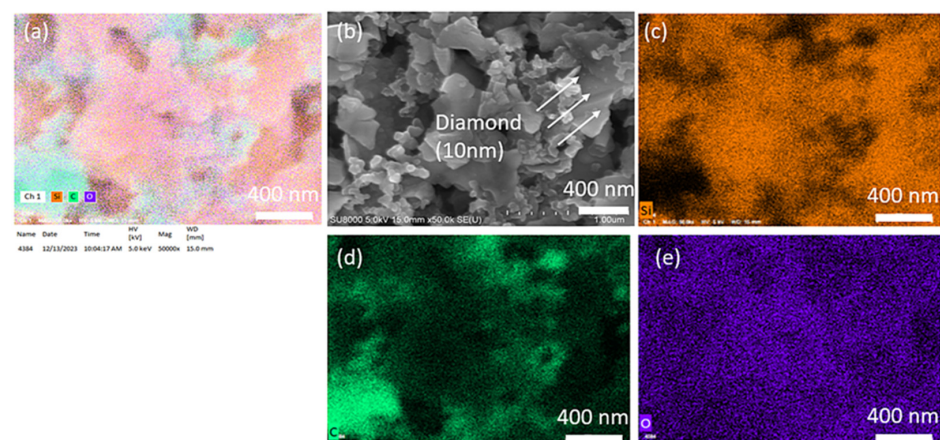


Figure 4. (a) Elemental mapping of Si-based anode with 3 wt.% 10 nm diamond, (b) SEM image of the surface of Si-based anode with 3 wt.% 10 nm diamond, (c) Si distribution, (d) C distribution, (e) O distribution of the surface of Si-based anode with 3 wt.% 10 nm diamond.

Figure 5a–d illustrates the surface microstructure and elemental distribution of the electrode without added nanodiamond powder after the 1st cycle of discharge and charge. Oxygen is represented in blue, silicon in red, carbon in green, and fluorine in yellow. In Figure 5a, multiple reaction hotspots emerge on the electrode surface due to uneven charge and discharge, leading to non-uniform growth of the solid electrolyte interphase (SEI) layer, resulting in significant surface irregularities. The reformation of SEI in these hotspot regions perpetuates the presence of microscopic cracks and defects. These fissures or flaws facilitate direct contact between silicon particles and the electrolyte. As depicted in Figure 5c, silicon exposed within these cracks exhibits higher fluorine contents, indicating secondary reactions between bare silicon and the electrolyte. Continuous reactions between silicon-based materials and LiPF₆ result in the formation of Li₂SiF₆ aggregates, a phenomenon previously documented by Fei Wei and colleagues [37].

Figure 5e–h depicts the surface microstructure and elemental distribution of the electrode with added nanodiamond powder after a single cycle of discharge and charge. The SEI layer on this sample's surface appears relatively uniform and devoid of prominent reaction hotspots. The elemental distribution in Figure 5g displays a more uniform pattern, indicating more homogeneous formation of the SEI layer with enhanced mechanical strength. No localized protrusions or cracks are observed on the sample [38].

Figure 5d,h shows zoomed-in images of the microstructures corresponding to Figure 5b,f. The microstructures exhibit similar morphology, with slight differences possibly arising from the rupture of the SEI in the electrode without a nanodiamond additive.

Figure 6a,c depicts the surface microstructure and elemental distribution of the electrode without added nanodiamond powder after undergoing 30 cycles. Oxygen, silicon, carbon, and fluorine are represented by blue, red, green, and yellow, respectively. Similar to the findings in Figure 6, the typical silicon anode surface displays protrusions larger than 10 µm after 30 cycles, indicating that silicon consequently decreased the overall electrochemical performance of the electrode. In contrast, the diamond powder-doped sample reveals a denser solid electrolyte interface (SEI) following 30 charge–discharge cycles that is free from protrusions exceeding 10 µm in size.

Following a single charge–discharge cycle, the electrode surfaces were exposed to an accelerating voltage of 5 kV for elemental composition analysis. The elemental ratios are shown in Table 1. As illustrated in Figure 6, the silicon anode without nanodiamond powder displayed a propensity for the formation of reactive hotspots, fostering thicker growth of the solid electrolyte interphase (SEI) within these areas. Originating from these focal points, micro-fractures became more prevalent, leading to silicon material exposure on the electrode surface. This increased silicon exposure readily triggered secondary reactions with the electrolyte, yielding Li₂SiF₆ and consequently augmenting the surface fluorine content [37].

Conversely, the electrode surface treated with supplemented nanodiamonds exhibited heightened mechanical strength and a more uniformly developed SEI. Herein, the surface silicon content measured at 1.8% was 0.42 times lower than that of the nanodiamond-free silicon anode. Additionally, the fluorine content demonstrated notably lower levels in comparison to the silicon anode devoid of nanodiamond additives. The electrode surface with fewer side reactions also exhibits lower fluorine content.

Figure 7 shows Cyclic voltammetry (CV) experiments conducted at a scanning rate of 0.1 mVs^{−1} aimed to uncover the electrochemical characteristics of the anodes. Throughout the discharge phase, two discernible peaks emerged at 0.18 V and 0.03 V, indicating the occurrence of Si–Li alloying processes. Moreover, during the charging phase, the appearance of two peaks at 0.35 V and 0.52 V signified de-alloying processes associated with the Li_xSi phase. The two samples exhibit similar cyclic voltammetry curves, with the characteristic peak positions being nearly identical [39].

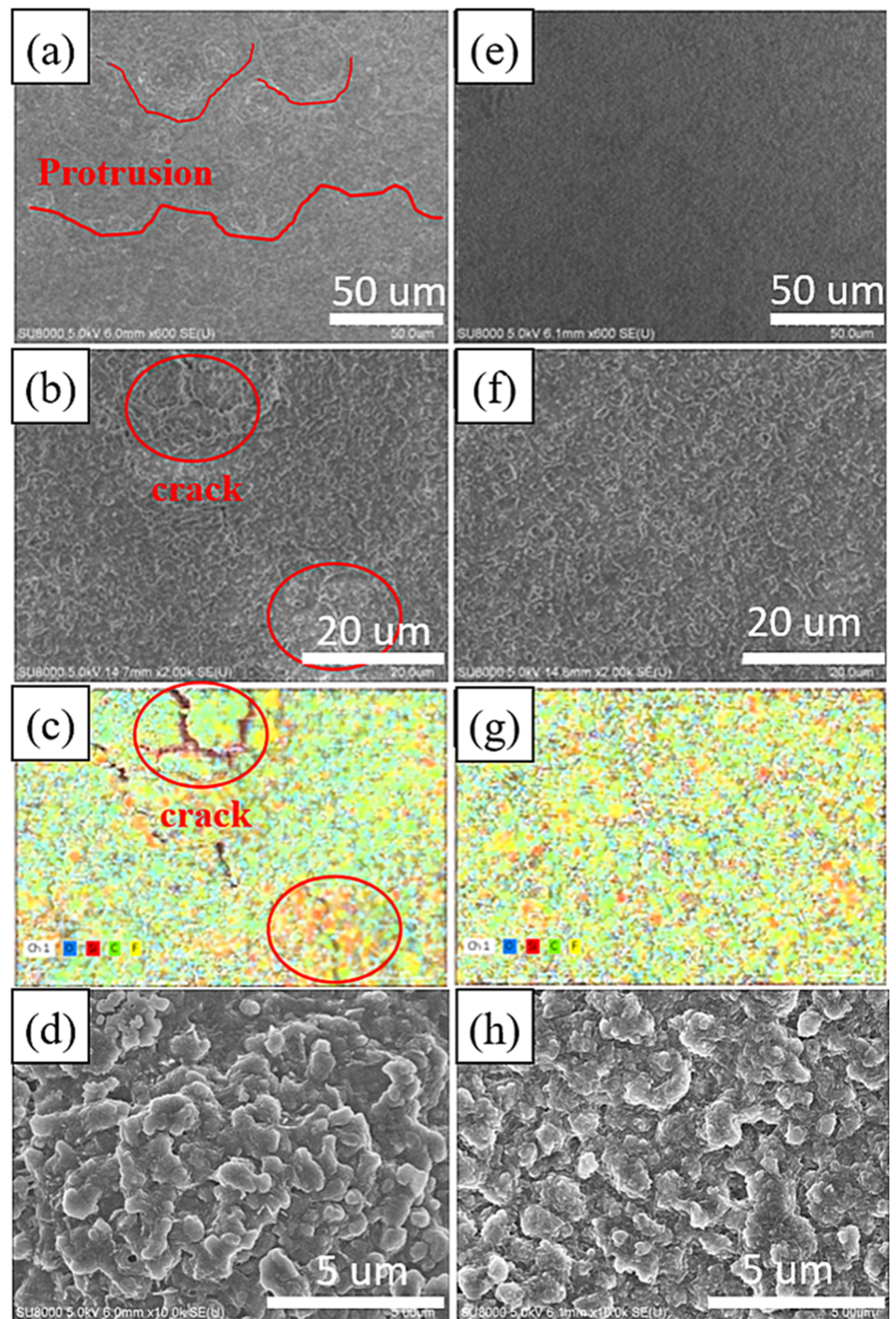


Figure 5. SEM image of the surface of 1st cycle Si-based anode after the 1st cycle (a,b,d), Si-based anode with nanocrystalline diamond (e,f,h) and elemental mapping of 1st cycle Si-based anode (c), and Si-based anode with nanocrystalline diamond (g).

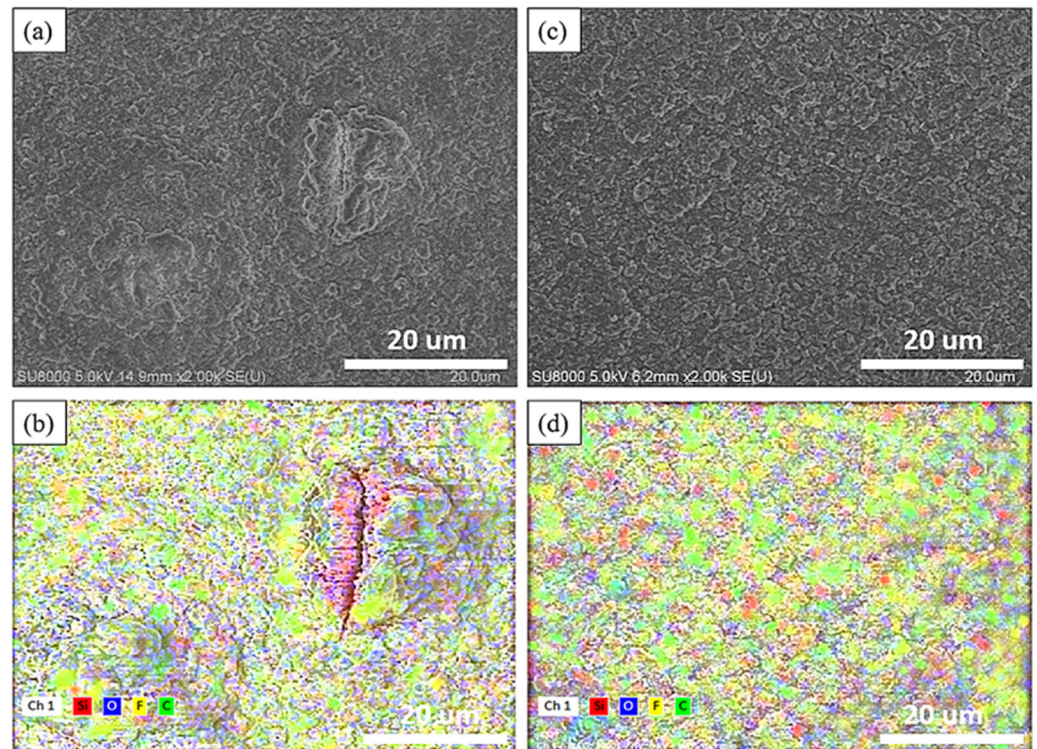


Figure 6. SEM image of the surface of 30th cycle Si-based anode (a) and Si-based anode with nanocrystalline diamond (c) Elemental mapping of 30th cycle Si-based anode (b) and Si-based anode with nanocrystalline diamond (d).

Table 1. Elemental composition of the surface of silicon-based anode and silicon-based anode modified by nanodiamonds.

Elemental Ratio (Atomic %)/Sample	Si	Si–Nanodiamond
C	22.7	21.4
O	68.9	75.3
F	4.17	1.51
Si	4.20	1.80

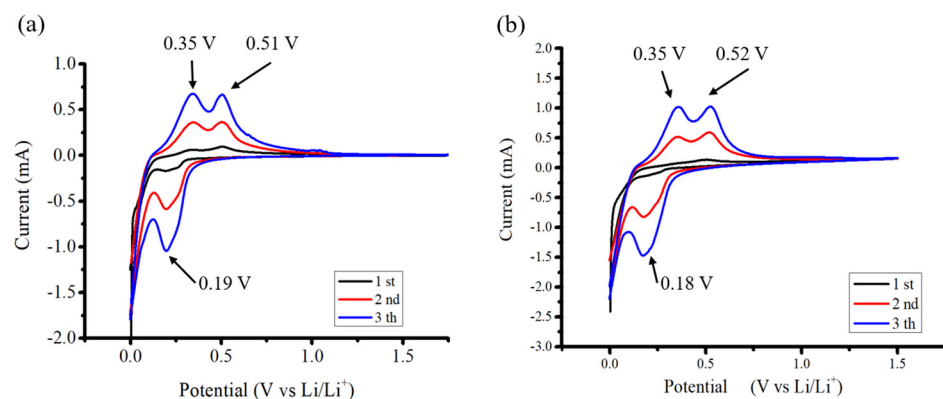


Figure 7. CV profiles of (a) Si flakes and (b) Si flakes with 10 nm ND.

The electrodes utilized in the study were uniformly loaded within the range of 0.9 to 1.0 mg/cm². The lithium storage characteristics of these electrodes were effectively evaluated via electrochemical analysis. The initial charge/discharge curves and the first Coulombic efficiency for various electrodes at a current density of 0.2 mA cm^{−2} are illustrated

in Figure 8. The Si-based anode demonstrated an initial capacity of 3565 mAh g^{-1} . Notably, the Si-based anode incorporating 10 and 30 nm NDs exhibited initial capacities of 3554 mAh g^{-1} and 3409 mAh g^{-1} , respectively. Moreover, the silicon anode without added nanodiamonds displayed a first-cycle Coulombic efficiency of 85.5%, whereas those integrated with 10 nm and 30 nm diamond powders exhibited Coulombic efficiencies of 83.0% and 75.1%, respectively. This notable decrease in first-cycle Coulombic efficiency is attributed to the substantial surface area of the nanodiamonds and the formation of partially irreversible compounds such as lithium carbonate on nanodiamond surfaces [40].

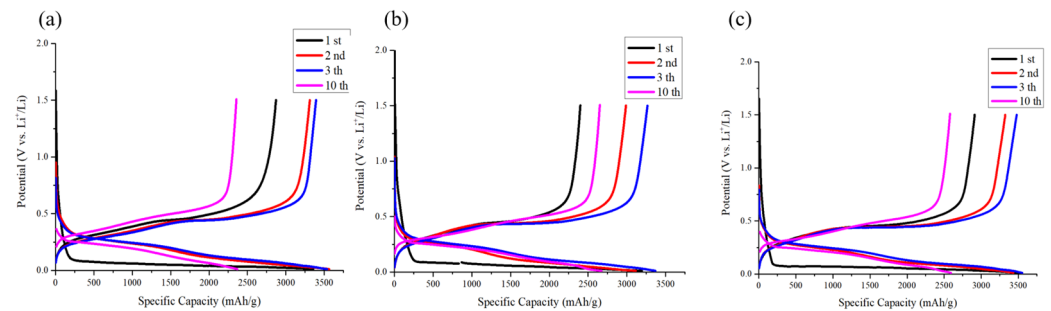


Figure 8. Voltage profile of anode comprising (a) Si flakes, (b) Si flakes with 3 wt.% nanodiamond (30 nm), and (c) Si flakes with 3 wt.% nanodiamond (10 nm).

As illustrated in Figure 9, during charge–discharge cycles, volume changes in nanosilicon particles lead to repeated rupture and reformation of the SEI layer. Silicon particles without nanodiamond additives exhibit uneven ion diffusion and often form reaction hotspots, resulting in capacity degradation. However, after 20 to 30 charge–discharge cycles, the electrode structure gradually stabilizes. Subsequently, the self-healing effect of the binder aids in gradual recovery of the electrode capacity.

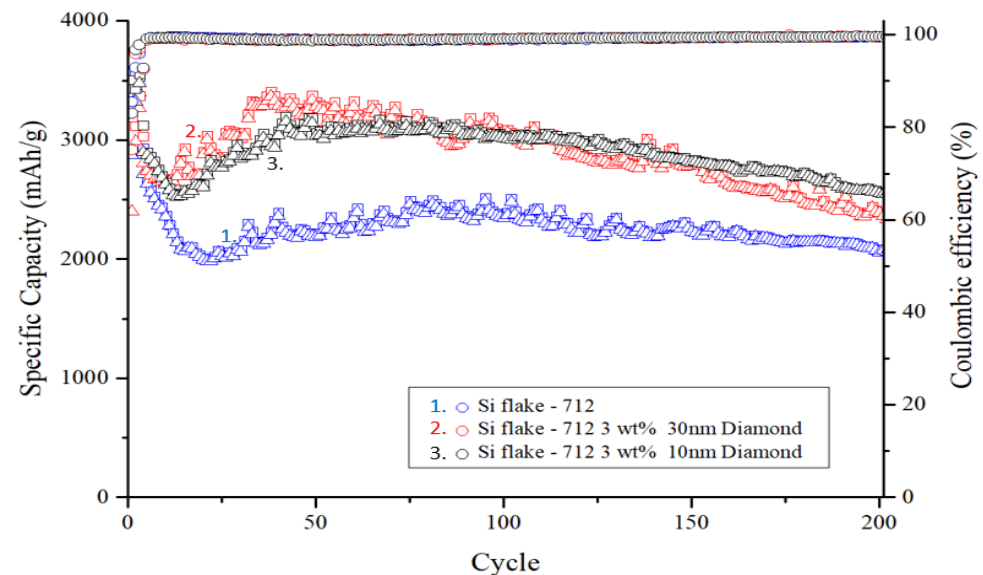


Figure 9. Cycle performance of silicon-based anode with and without nanodiamond.

The square in Figure 9 represents the discharge capacity of the anode for that cycle, while the triangle indicates the charge capacity. The Coulombic efficiency, represented by the circle, is calculated by dividing the charge capacity by the discharge capacity.

The electrode containing nanodiamond particles also displayed a trend of capacity rebound. The addition of nanodiamonds resulted in reduced decay of the initial capacity owing to the absence of reaction hotspots. This observation suggests that the surface functional groups and compounds present in nanodiamonds contribute to capacity rebound

and facilitate self-healing of damage to the PAA binder, particularly amidst the significant volume expansion during silicon–lithium alloying.

Upon completion of 200 charge–discharge cycles, the silicon anode devoid of added nanodiamonds retained only 2063 mAh g^{-1} , representing a capacity retention rate of 58.1% compared with its initial capacity. Conversely, silicon anodes with an added 10 nm and 30 nm of polycrystalline nanodiamond particles maintained high capacities of 2597 mAh g^{-1} and 2340 mAh g^{-1} , respectively, with capacity retention rates of 74.2% and 69.5% after prolonged cycling.

Figure 10 illustrates the rate capability of electrodes ranging from 0.2 to 4 mA cm^{-2} . Remarkably, the Si-based anode with nanodiamonds exhibited notable capacity (1010 mAh g^{-1}) even at 4 mA cm^{-2} , which can be attributed to its exceptional structural stability and the presence of a uniform solid electrolyte interphase (SEI) layer. Of note, from the rate-performance curves was the observation of a flatter voltage plateau for the Si-based anode with nanodiamonds, which is indicative of reduced polarization at higher test currents [41].

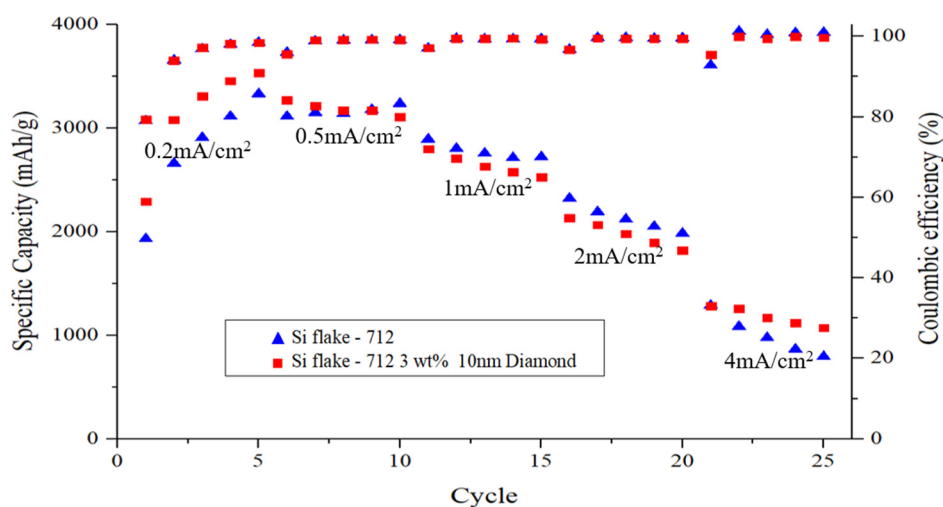


Figure 10. C-rate step test of silicon-based anode with or without nanodiamond.

When silicon is mixed with diamond nanoparticles, it results in the formation of a uniform and thinner solid electrolyte interphase (SEI) layer compared with pristine silicon-based anode. This implies reduced breakdown of the electrolyte in the former scenario. Even after undergoing 200 cycles, there is no observable alteration in the morphology of the Si–nanodiamond anode, which maintains a notably thinner SEI layer, as shown in Figure 8.

For a more comprehensive understanding of the system and to validate the characteristics of the SEI layer, electrochemical impedance spectroscopy (EIS) was conducted after the initial cycle. Figure 11 illustrates these spectra alongside the equivalent circuit model. Within this schematic, R1 denotes the ohmic series resistance of the cell components, R2 represents the Li ion transfer resistance through the SEI layer, and R3 signifies the charge transfer resistance. W1 pertains to the Warburg impedance linked to the diffusion of Li ions into the active electrode. The elements C1, C2, and C3 stand for constant phase elements, replacing traditional capacitor components [42,43]. Furthermore, the equivalent circuit incorporates the Li electrode component, acknowledging its influence on the overall impedance. The addition of diamond nanoparticles evidently reduces resistance, fostering an environment conducive to the alloying and de-alloying of lithium with silicon flakes.

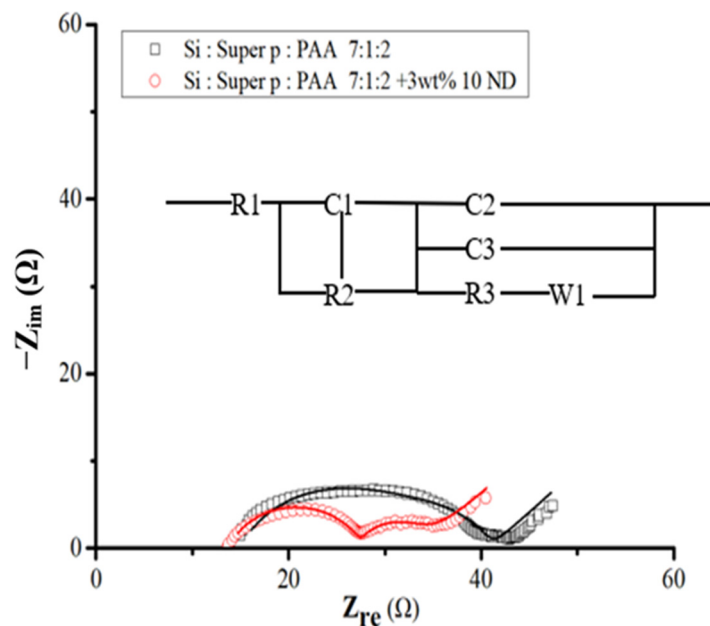


Figure 11. EIS spectra for Si- and Si–nanodiamond-based anodes after one cycle of discharge and charge and the equivalent circuit diagram corresponding to the EIS curves.

Following the fitting process, Table 2 shows the SEI layer impedance, R2, and charge transfer impedance, R3, for Si–nanodiamond electrodes to be 14 Ω and 7 Ω respectively, contrasting with the higher values of 18 Ω and 8 Ω obtained from pristine silicon samples. The observed increase in resistance, depicted by enlargement of the semicircle in the spectra shown in Figure 11, is more pronounced in the case of pristine silicon. Moreover, the significantly lower R2 observed in Si–nanodiamond-based anode can be attributed to the presence of a uniform and thinner SEI layer, an inference drawn from electrochemical characterizations.

Table 2. Derived elemental resistance in the equivalent circuit by best fitting to the EIS curves of the pristine Si and Si–nanodiamond electrodes.

Elemental Ratio (Atomic %)/Sample	Si	Si–Nanodiamond
R1	15	14
R2	18	14
R3	8	7

EIS analyses were carried out on samples after 30 cycles, as shown in Figure 12, which presents Nyquist impedance plots of activated Si flakes and Si ND composite materials. Notably, both samples demonstrated a more stabilized electrode interface after the 30 cycles. Specifically, the charge transfer resistance related to the electrochemical reaction and the resistance of the SEI (solid electrolyte interphase) interface decreased to 5 ohms (R2), while the contact resistance reached 8 ohms in electrodes enriched with nanodiamond powder. These findings are shown in Table 3 and are consistent with the results of prolonged cycling studies, highlighting the positive impact of nanodiamond powder on enhancement of the stability of the solid electrolyte interphase layer.

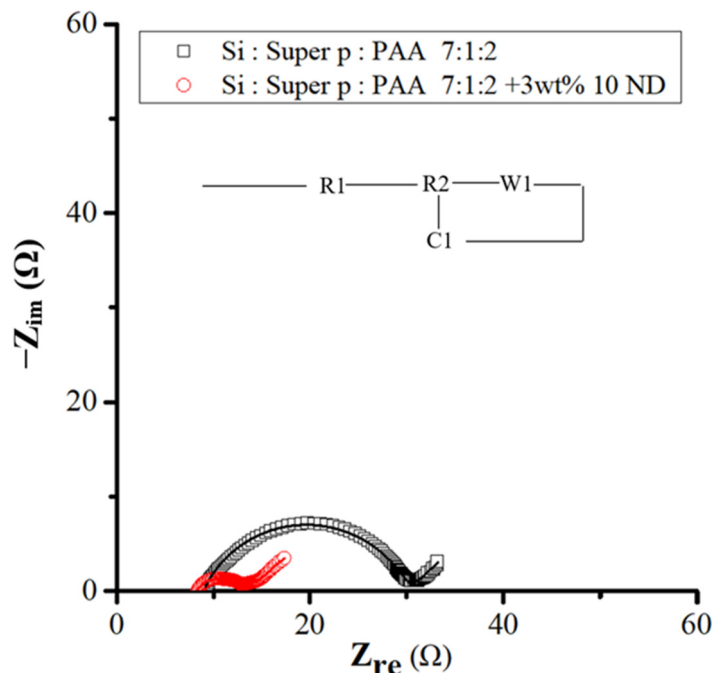


Figure 12. EIS spectra for Si- and Si-nanodiamond-based anodes after the 30th cycle of discharge and charge and the equivalent circuit diagram corresponding to the EIS curves.

Table 3. Derived elemental resistance in the equivalent circuits by best fitting to the EIS curves of the pristine Si and Si-nanodiamond electrodes after the 30th cycle.

Elemental Ratio (Atomic %)/Sample	Si	Si-Nanodiamond
R1	9	8
R2	21	5

Figure 13 illustrates the formation of the solid electrolyte interphase (SEI) layer on both silicon and silicon-nanodiamond composite electrodes. The electrode without nanodiamond tends to develop reaction hotspots, leading to the uneven growth of the local SEI layer. Areas with excessive SEI growth are prone to structural defects, resulting in the exposure of fresh silicon material. Exposed silicon further reacts with the electrolyte, thereby compromising the electrochemical performance of the electrode.

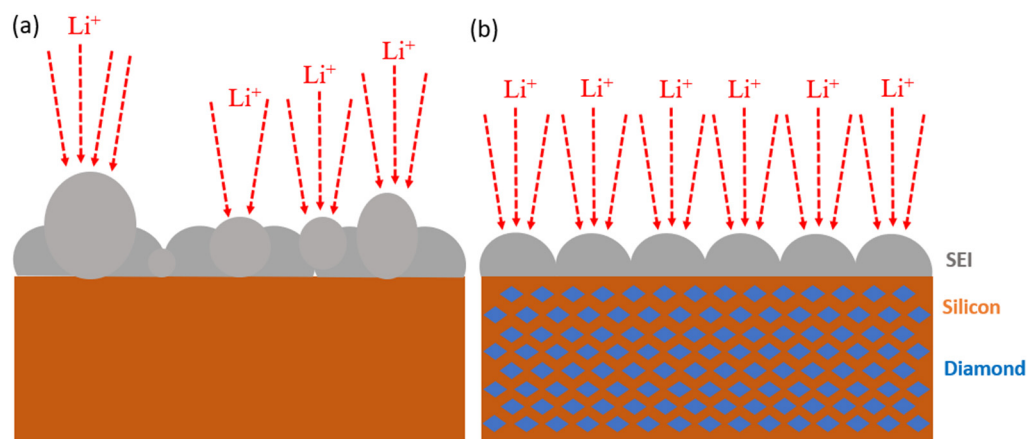


Figure 13. Schematic illustration of SEI layer formation in (a) pristine Si and (b) Si-nanodiamond electrodes after 1st cycle of discharge and charge.

In contrast, the silicon–nanodiamond composite electrode exhibits a more uniform SEI layer, demonstrating superior mechanical properties. The surface of the composite electrode does not exhibit micrometer-scale agglomerations or cracks, indicating excellent structural stability and favorable electrochemical characteristics.

4. Conclusions

The performance of a silicon-based negative electrode is significantly improved by adding nanodiamonds of 10 nm or 30 nm in size to micrometer-scale silicon flake. A uniform and robust solid electrolyte interphase (SEI) layer was formed by the aid of nanodiamonds, thereby improving the mechanical stability and enhancing the high-rate discharge capabilities of the battery while extending its cycle life.

Scanning electron microscopy (SEM), Raman spectroscopy, X-ray diffraction (XRD), and electrochemical tests revealed that even after 200 charge–discharge cycles, the electrode maintained a capacity of 75% and sustained a specific capacity exceeding 1000 mAh g^{−1} under a high testing current of 4 mA cm^{−2}. This underscores the continuous stability achieved in the SEI layer through the integration of nanodiamonds with silicon-based negative electrodes, resulting in improved cycling stability and advancements in rapid charge–discharge performance.

In brief, this paper presents an effective strategy involving the utilization of nanodiamond additives to a silicon-flake-based anode of a lithium-ion battery to significantly improve anode performance. Nanodiamonds are inexpensive and abundant. We believe that this paper will inspire many further research efforts in the application of nanodiamonds to achieve much higher performance in lithium-ion batteries and beyond.

Author Contributions: Conceptualization, Y.T. and C.-Y.J.; methodology, Y.T. and C.-Y.J.; validation, C.-Y.J. and S.-H.S.; formal analysis, Y.T., C.-Y.J. and S.-H.S.; investigation, Y.T., C.-Y.J. and S.-H.S.; resources, Y.T.; data curation, C.-Y.J. and S.-H.S.; writing—original draft preparation, C.-Y.J.; writing—review and editing, Y.T.; visualization, C.-Y.J. and S.-H.S.; supervision, Y.T. and C.-Y.J.; project administration, Y.T.; funding acquisition, Y.T. All authors have read and agreed to the published version of the manuscript.

Funding: This research was funded by the National Science and Technology Council in Taiwan, grant number 112-2221-E-006-075 -.

Data Availability Statement: Data are contained within the article.

Acknowledgments: The authors gratefully acknowledge the use of code XRD005100 of the machine equipment belonging to the Core Facility Center of National Cheng Kung University and the use of the scanning electron microscope (SEM, Hitachi-SU8000, Taipei, Taiwan), and the ultrahigh Resolution Transmission Electron Microscope (STEM JEOL-2100F CS, Taipei, Taiwan) provided by the Instrument Center of National Cheng Kung University.

Conflicts of Interest: The authors declare no conflict of interest.

References

1. Kim, T.; Song, W.; Son, D.-Y.; Ono, L.K.; Qi, Y. Lithium-ion batteries: Outlook on present, future, and hybridized technologies. *J. Mater. Chem. A* **2019**, *7*, 2942–2964. [[CrossRef](#)]
2. Li, M.; Lu, J.; Chen, Z.; Amine, K. 30 years of lithium-ion batteries. *Adv. Mater.* **2018**, *30*, 1800561. [[CrossRef](#)] [[PubMed](#)]
3. Blomgren, G.E. The development and future of lithium ion batteries. *J. Electrochem. Soc.* **2016**, *164*, A5019.
4. Zubi, G.; Dufo-López, R.; Carvalho, M.; Pasaoglu, G. The lithium-ion battery: State of the art and future perspectives. *Renew. Sustain. Energy Rev.* **2018**, *89*, 292–308.
5. Wee, J.H. A feasibility study on direct methanol fuel cells for laptop computers based on a cost comparison with lithium-ion batteries. *J. Power Sources* **2007**, *173*, 424–436. [[CrossRef](#)]
6. Lu, L.; Han, X.; Li, J.; Hua, J.; Ouyang, M. A review on the key issues for lithium-ion battery management in electric vehicles. *J. Power Sources* **2016**, *226*, 272–288. [[CrossRef](#)]
7. Wood, D.L., III; Li, J.; Daniel, C. Prospects for reducing the processing cost of lithium ion batteries. *J. Power Sources* **2015**, *275*, 234–242. [[CrossRef](#)]
8. Zhang, H.; Yang, Y.; Ren, D.; Wang, L.; He, X. Graphite as anode materials: Fundamental mechanism, recent progress and advances. *Energy Storage Mater.* **2021**, *36*, 147–170. [[CrossRef](#)]

9. Tokumitsu, K.; Fujimoto, H.; Mabuchi, A.; Kasuh, T. High capacity carbon anode for Li-ion battery: A theoretical explanation. *Carbon* **1999**, *37*, 1599–1605. [[CrossRef](#)]
10. Su, X.; Wu, Q.; Li, J.; Xiao, X.; Lott, A.; Lu, W.; Sheldon, B.W.; Wu, J. Silicon-based nanomaterials for lithium-ion batteries: A review. *Adv. Energy Mater.* **2014**, *4*, 1300882. [[CrossRef](#)]
11. Zhu, B.; Wang, X.; Yao, P.; Li, J.; Zhu, J. Towards high energy density lithium battery anodes: Silicon and lithium. *Chem. Sci.* **2019**, *10*, 7132–7148. [[CrossRef](#)] [[PubMed](#)]
12. Jin, Y.; Zhu, B.; Lu, Z.; Liu, N.; Zhu, J. Challenges and recent progress in the development of Si anodes for lithium-ion battery. *Adv. Energy Mater.* **2017**, *7*, 1700715. [[CrossRef](#)]
13. Sun, L.; Liu, Y.; Shao, R.; Wu, J.; Jiang, R.; Jin, Z. Recent progress and future perspective on practical silicon anode-based lithium ion batteries. *Energy Storage Mater.* **2022**, *46*, 482–502. [[CrossRef](#)]
14. Chen, X.; Li, H.; Yan, Z.; Cheng, F.; Chen, J. Structure design and mechanism analysis of silicon anode for lithium-ion batteries. *Sci. China Mater.* **2019**, *62*, 1515–1536. [[CrossRef](#)]
15. Franco Gonzalez, A.; Yang, N.H.; Liu, R.S. Silicon anode design for lithium-ion batteries: Progress and perspectives. *J. Phys. Chem. C* **2017**, *121*, 27775–27787. [[CrossRef](#)]
16. Zhang, C.; Wang, F.; Han, J.; Bai, S.; Tan, J.; Liu, J.; Li, F. Challenges and recent progress on silicon-based anode materials for next-generation lithium-ion batteries. *Small Struct.* **2021**, *2*, 2100009. [[CrossRef](#)]
17. De las Casas, C.; Li, W. A review of application of carbon nanotubes for lithium ion battery anode material. *J. Power Sources* **2012**, *208*, 74–85. [[CrossRef](#)]
18. Wu, Y.P.; Rahm, E.; Holze, R. Carbon anode materials for lithium ion batteries. *J. Power Sources* **2003**, *114*, 228–236. [[CrossRef](#)]
19. Landi, B.J.; Ganter, M.J.; Cress, C.D.; DiLeo, R.A.; Raffaele, R.P. Carbon nanotubes for lithium ion batteries. *Energy Environ. Sci.* **2009**, *2*, 638–654. [[CrossRef](#)]
20. Pan, Q.; Wang, H.; Jiang, Y. Covalent modification of natural graphite with lithium benzoate multilayers via diazonium chemistry and their application in lithium ion batteries. *Electrochem. Commun.* **2007**, *9*, 754–760. [[CrossRef](#)]
21. Song, J.; Zhou, M.; Yi, R.; Xu, T.; Gordin, M.L.; Tang, D.; Yu, Z.; Regula, M.; Wang, D. Interpenetrated gel polymer binder for high-performance silicon anodes in lithium-ion batteries. *Adv. Funct. Mater.* **2014**, *24*, 5904–5910. [[CrossRef](#)]
22. Shin, J.; Cho, E. Agglomeration mechanism and a protective role of Al₂O₃ for prolonged cycle life of Si anode in lithium-ion batteries. *Chem. Mater.* **2018**, *30*, 3233–3243. [[CrossRef](#)]
23. Nunn, N.; Torelli, M.; McGuire, G.; Shenderova, O. Nanodiamond: A high impact nanomaterial. *Curr. Opin. Solid State Mater. Sci.* **2017**, *21*, 1–9. [[CrossRef](#)]
24. Mochalin, V.N.; Gogotsi, Y. Nanodiamond–polymer composites. *Diam. Relat. Mater.* **2015**, *58*, 161–171. [[CrossRef](#)]
25. Mochalin, V.; Shenderova, O.; Ho, D.; Gogotsi, Y. The properties and applications of nanodiamonds. In *Nano-Enabled Medical Applications*; Jenny Stanford Publishing: Singapore, 2020; pp. 313–350.
26. Wang, C.; Sun, X.; Zhang, X.; Li, H. Introducing nanodiamonds in electrolyte and SEI for highly improving performances of lithium-ion batteries. *Appl. Surf. Sci.* **2022**, *600*, 154178. [[CrossRef](#)]
27. Feng, K.; Li, M.; Liu, W.; Kashkooli, A.G.; Xiao, X.; Cai, M.; Chen, Z. Silicon-based anodes for lithium-ion batteries: From fundamentals to practical applications. *Small* **2018**, *14*, 1702737. [[CrossRef](#)] [[PubMed](#)]
28. Ashuri, M.; He, Q.; Shaw, L.L. Silicon as a potential anode material for Li-ion batteries: Where size, geometry and structure matter. *Nanoscale* **2016**, *8*, 74–103. [[CrossRef](#)]
29. Ko, M.; Chae, S.; Cho, J. Challenges in accommodating volume change of Si anodes for Li-ion batteries. *ChemElectroChem* **2015**, *2*, 1645–1651. [[CrossRef](#)]
30. Chae, S.; Ko, M.; Kim, K.; Ahn, K.; Cho, J. Confronting issues of the practical implementation of Si anode in high-energy lithium-ion batteries. *Joule* **2017**, *1*, 47–60. [[CrossRef](#)]
31. Tzeng, Y.; Jhan, C.Y.; Wu, Y.H. Effects of pyrolysis on high-capacity Si-based anode of lithium ion battery with high coulombic efficiency and long cycling life. *Nanomaterials* **2022**, *12*, 469. [[CrossRef](#)]
32. Mermoux, M.; Chang, S.; Girard, H.A.; Arnault, J.C. Raman spectroscopy study of detonation nanodiamond. *Diam. Relat. Mater.* **2018**, *87*, 248–260. [[CrossRef](#)]
33. Klauser, F.; Steinmüller-Nethl, D.; Kaindl, R.; Bertel, E.; Memmel, N. Raman studies of nano- and ultra-nanocrystalline diamond films grown by hot-filament CVD. *Chem. Vap. Depos.* **2010**, *16*, 127–135. [[CrossRef](#)]
34. Piscanec, S.; Cantoro, M.; Ferrari, A.C.; Zapien, J.A.; Lifshitz, Y.; Lee, S.T.; Hofmann, S.; Robertson, J. Raman spectroscopy of silicon nanowires. *Phys. Rev. B* **2003**, *68*, 241312. [[CrossRef](#)]
35. Tzeng, Y.; He, J.L.; Jhan, C.Y.; Wu, Y.H. Effects of SiC and Resorcinol–Formaldehyde (RF) Carbon Coatings on Silicon-Flake-Based Anode of Lithium Ion Battery. *Nanomaterials* **2021**, *11*, 302. [[CrossRef](#)] [[PubMed](#)]
36. Osipov, V.Y.; Shakhov, F.M.; Bogdanov, K.V.; Takai, K.; Hayashi, T.; Treussart, F.; Baldycheva, A.; Hogan, B.T.; Jentgens, C. High-quality green-emitting nanodiamonds fabricated by HPHT sintering of polycrystalline shockwave diamonds. *Nanoscale Res. Lett.* **2020**, *15*, 209. [[CrossRef](#)] [[PubMed](#)]
37. Yu, C.; Chen, X.; Xiao, Z.; Lei, C.; Zhang, C.; Lin, X.; Shen, B.; Zhang, R.; Wei, F. Silicon carbide as a protective layer to stabilize Si-based anodes by inhibiting chemical reactions. *Nano Lett.* **2019**, *19*, 5124–5132. [[CrossRef](#)] [[PubMed](#)]

38. Li, Y.; Jin, B.; Wang, K.; Song, L.; Ren, L.; Hou, Y.; Gao, X.; Zhan, X.; Zhang, Q. Coordinatively-intertwined dual anionic polysaccharides as binder with 3D network conducive for stable SEI formation in advanced silicon-based anodes. *Chem. Eng. J.* **2020**, *429*, 132235. [[CrossRef](#)]
39. Shao, R.; Zhu, F.; Cao, Z.; Zhang, Z.; Dou, M.; Niu, J.; Zhu, B.; Wang, F. Heteroatom-doped carbon networks enabling robust and flexible silicon anodes for high energy Li-ion batteries. *J. Mater. Chem. A* **2020**, *8*, 18338–18347. [[CrossRef](#)]
40. Liang, B.; Zhang, L.; Wang, W.; Xu, G.; Zhang, W.; Zhang, Y.; Zhang, R.; Yang, L.; Zhang, L. Nanodiamond core/onion-like carbon shell materials with excellent visible light photocatalytic activity. *Mater. Res. Express* **2019**, *6*, 045609. [[CrossRef](#)]
41. Wu, M.; Song, X.; Liu, X.; Battaglia, V.; Yang, W.; Liu, G. Manipulating the polarity of conductive polymer binders for Si-based anodes in lithium-ion batteries. *J. Mater. Chem. A* **2015**, *3*, 3651–3658. [[CrossRef](#)]
42. Wu, C.C.; Li, C.C. Distribution uniformity of water-based binders in si anodes and the distribution effects on cell performance. *ACS Sustain. Chem. Eng.* **2020**, *8*, 6868–6876. [[CrossRef](#)]
43. Paloukis, F.; Elmasides, C.; Farmakis, F.; Selinis, P.; Neophytides, S.G.; Georgoulas, N. Electrochemical Impedance Spectroscopy study in micro-grain structured amorphous silicon anodes for lithium-ion batteries. *J. Power Sources* **2016**, *331*, 285–292. [[CrossRef](#)]

Disclaimer/Publisher’s Note: The statements, opinions and data contained in all publications are solely those of the individual author(s) and contributor(s) and not of MDPI and/or the editor(s). MDPI and/or the editor(s) disclaim responsibility for any injury to people or property resulting from any ideas, methods, instructions or products referred to in the content.